J Mater Sci (2006) 41:7425–7436
DOI 10.1007/s10853-006-0808-y

Oxide ceramic laminates with highly textured α-alumina interlayers: I. Texture control and laminate formation

Ming Wei · Dan Zhi · David G. Brandon

Received: 18 August 2005 / Accepted: 29 November 2005 / Published online: 20 September 2006

Abstract Three kinds of texture-reinforced oxide ceramic laminates with strongly bonded interfaces have been fabricated. All three were based on highly textured α-alumina interlayers, but each with a different oxide laminate matrix and a correspondingly different thermal mismatch between the textured interlayers and the matrix. Alginate-based, aqueous gel casting was used to produce a flexible tape for all the compositions studied. The highly textured alumina (TA) interlayers were derived from gel-cast tapes containing aligned alumina seed platelets. It has been found that the strongest texture derived from 9.1 vol% of the seed platelets in the gelled precursor tape. Using the March–Dollase model for texture analysis, the oriented volume fraction in the highly textured interlayers was estimated to vary from 60 to 80%.

Introduction

In a conventional ceramic the anisotropic single crystal properties are averaged in the isotropic, randomly oriented polycrystal. Texturing a polycrystalline material, by controlling the orientation distribution of crystallites with respect to the coordinate system of a component, could be used to tailor electronic and structural properties and obtain some of the single crystal anisotropy. Such texture could be used to reduce thermal expansion mismatch, and hence the risk of microcracking [1], while texture control offers a useful alternative to aligned second-phase reinforcement [2]. Most recently, it has been reported that the formation of texture in α-alumina can effectively lower the residual stress and make the stress distribution narrower [3]. In general, processing to develop texture in ceramics differs significantly from the conventional powder processing of dense, fine-grained and equiaxed microstructures. Textured ceramics have been fabricated by several techniques: sinter-forging [4], hot-pressing [5], slip-casting [6], gel-casting in a magnetic field [1, 7, 8], and, most commonly, by 'templating', using seeded grain growth [2, 9–13]. Textured microstructures have been reported in a single-phase iron titanate ceramic laminate, containing a predetermined configuration of the textured and non-textured layers [8].

The design of ceramic composites with layered macrostructures is also receiving considerable research attention because they exhibit decreased sensitivity to surface defects and have demonstrated non-catastrophic failure in some laminate systems [14–16]. A key feature in multilayer ceramic systems is the ability to deflect propagating cracks and two different mechanisms of crack deflection have previously been employed. Propagating cracks can be deflected either along weak interfaces with adjacent layers [14, 15] or into layers exhibiting residual biaxial compressive stress [17–19]. Essentially, the first mechanism depends on matrix/interface strength ratio and has had varying degrees of success. However, controlling the strength

M. Wei (✉) · D. Zhi
Department of Materials Science and Metallurgy, University of Cambridge, Cambridge CB2 3QZ, UK
e-mail: dr.m.wei@gmail.com

D. G. Brandon
Department of Materials Engineering, Technion – Israel Institute of Technology, Haifa 32000, Israel

of such ceramics is technologically difficult, and furthermore weak interfaces are known to compromise certain properties. The use of residual stress patterns associated with thermal expansion mismatch within ceramic laminate materials therefore offers an attractive alternative mechanism to improve fracture behaviour.

In the present research, texture-reinforced oxide ceramic laminates have been prepared by an alginate-based, gel-cast, doctor-blade process, in which tape lay-ups to develop the laminated structure. Three laminate systems were studied; all based on strongly bonded interfaces between the matrix composition and highly textured alumina (TA) interlayers. The control of mechanical anisotropy by the presence of strongly bonded and textured interlayers is independent of, and quite different from, the principle of reinforcement by weak-interface crack deflection, which is used to inhibit through-thickness crack propagation in many aligned ceramic composites.

In this paper, the texture and microstructure of the alumina interlayers were optimized by controlling the volume fraction and alignment of alumina seed platelets in a precursor tape. Meanwhile, three types of matrix layer were used in three laminate systems:

1. A reaction-bonded aluminum oxide (RBAO), designed for minimum sintering shrinkage and a near-zero residual thermal stress in the fully sintered, single-phase alumina/TA laminate.
2. An alumina-toughened zirconia (ATZ), designed for minimum tetragonal zirconia grain-size and with controlled residual tension in the zirconia matrix layers of the laminate.
3. A reaction-bonded (zircon-based) mullite (RBM), designed for maximum mullite conversion and residual compression in the mullite matrix layers of the laminate.

This paper reports the processing methodology and texture control for these three texture-reinforced ceramic laminates. It will be followed by a further report on microstructural development and mechanical behaviour of the three laminate systems.

Experimental procedure

Powder preparation

A high purity, submicron α-Al_2O_3 powder (Ceralox, HPA-0.5) and a known volume percent of α-Al_2O_3 seed platelets (10–15 μm diameter, ELF Atochem) were used to prepare the TA layers. The oxide matrix precursor powder compositions and their sources are listed in Table 1. The RBAO powder mixture was attrition-milled in acetone with 3 mm-diameter high-purity Al_2O_3 beads (99.9%, Union Process) for 6–8 h at 500–600 rpm. After drying in a ventilation hood, the powder mixture was sieved with a 60-mesh sieve. The particle size of the RBAO powder before and after attrition milling was monitored by scanning electron microscopy (LEO 982) and laser particle size analysis (HORIBA, LA-910).

Gel casting and lamination

Water-based gel casting [2] was used to fabricate both the textured and texture-free layers. An in situ sol-gel reaction based on ion exchange between water-soluble sodium alginate and polyvalent cations yields an insoluble, cation cross-linked alginate gel:

$$\mathrm{Na}_n\text{alginate} + n/2\mathrm{Ca}^{2+} \rightarrow n\mathrm{Na}^{+} + \mathrm{Ca}_{n/2}\,\text{alginate} \quad (1)$$

A 0.15 M Ca^{2+} solution of calcium nitrate-4-hydrate (AR purity, Riedel-deHaën), served as the gelling solution. The seeded alumina layers were prepared by first mixing the alumina powder with alginate and a dispersant in distilled water by ball milling in a plastic bottle for at least 12 h (99.9% alumina balls, 5 mm diameter—Union Process). The alumina seed platelets were then incorporated and ball-milled for a further 5 h. The homogeneously mixed slip was transferred to a second plastic bottle to remove the alumina balls, and then rolled slowly on the ball mill for about 2 h to remove trapped air bubbles. The de-gassed slips were poured into the tape caster and cast with the gelling solution onto a Mylar sheet substrate (Dupont) which

Table 1 Precursor powders for RBAO, ATZ and RBM layers

Layer type	Material	Powder characteristic and source	Composition (wt%)
RBAO	Al	Globular, 99.36%, 45–90 mm, Miller Thermal, Inc.	20–40
	Al_2O_3	Submicron, Ceralox, HPA-0.5	60–80
ATZ	TZ3Y20A	TSK, Y-stabilized tetragonal ZrO_2 + α-Al_2O_3, <100 nm	ZrO_2 (75.2) Y_2O_3 (4.2) Al_2O_3 (20)
RBM	$ZrSiO_4$*	submicron, Rami Submicron,	54.5
	Al_2O_3	Ceralox, HPA-0.5	45.5

* Another zircon powder (~5 mm) was used for comparison

was supported on an inclined glass plate to drain away excess gelling solution and inhibit premature gelling of the slip beneath the doctor blade. The thickness of the cast tape was controlled by adjusting both the caster velocity and the gap between the extended doctor blade and the casting plate. Strong, flexible green tapes 100–200 μm in thickness were obtained with a doctor blade gap of 250 μm.

The non-textured oxide layers (RBAO, ATZ, and RBM) were cast by an identical gel-casting process, but without incorporation of the seed platelets. The slip compositions for the TA layers and the three types of non-textured oxide layers are listed in Table 2.

After casting, the tapes were detached from the Mylar sheet, by inverting the substrate in a distilled water bath. The tapes were then washed to remove excess cation, and 1.25″ diameter disks were stamped from the washed tapes using a polished steel punch (Buehler). Green laminate specimens were pressed from a stacked lay-up of the textured and non-textured disks in a stainless steel die (also 1.25″ in diameter), using a single filter paper top and bottom to prevent adhesion and allow excess water to escape. The specimens were uniaxially pressed in the die at ~80 Mpa for 20 min and subsequently cold isostatically pressed (CIP) at 250–300 MPa for 30 min.

Sintering

Residual water was removed by drying in a 2.45 GHz microwave oven (EM-S301, SANYO) operated at 100–150 W for 30–60 min. The progress of microwave drying was assessed by weighing the samples. The small quantity of organic additives (<1 vol% of dispersant and alginate) was removed during the sintering/reaction-bonding cycle and not as a separate burnout treatment.

As previously reported for monolithic RBAO ceramic processing [20–23], a somewhat complex heating cycle is required to sinter the RBAO/TA laminates to high density (avoiding swelling) and with 100% conversion to oxide. Oxidation of the aluminum metal particles at low temperatures (below the melting point) is essential and was accomplished by an initially low heating rate (1 °C/min) and low temperature hold (600 °C, 4–10 h). The green RBAO/TA laminated samples were placed on a porous alumina tile to ensure free oxygen access beneath the sample during reaction bonding.

The alumina-toughened zirconia/textured alumina (ATZ/TA) and reaction-bonded mullite/textured alumina (RBM/TA) laminates were sintered conventionally. Dissociation of zircon and its reaction with alumina to form zirconia and mullite only occurs above 1400 °C [24], so the heating cycle selected for the RBM laminates was 5°/min up to 1400 °C, 2°/min from 1400 to1600 °C, followed by holding for 5 h at 1600 °C and then cooling to room temperature at 5 °C/min. The effect of the zircon particle size on the phase evolution of the RBM layers was evaluated by X-ray diffraction phase analysis and the final density of the laminate composite samples was determined by Archimedes density measurements.

Texture characterization

The chemical homogeneity and composition of individual grains were determined from carbon-coated, polished and thermally etched samples using conventional scanning electron microscopy (SEM) and energy dispersive X-ray spectroscopy (EDS—JEOL 840). The microstructure of cross-sections taken from laminated samples was also examined by diffraction contrast transmission electron microscopy (TEM-JEOL 2000-FX) at 200 kV. TEM samples were prepared by diamond-sectioning perpendicular to the original plane of the precursor tape, followed by mechanical grinding, dimpling, and precision ion polishing (PIPS—Gatan, Model 691).

The Harris method [25–27] was used to quantify the degree of crystallographic alignment (texture) in all specimens. X-ray diffraction spectra were taken from polished surfaces prepared parallel to the direction of tape casting. Reference diffraction data were obtained from randomly oriented high purity alumina powder (HPA-0.5, Ceralox). All X-ray data were collected on an X-ray diffractometer with a

Table 2 Slip composition for gel casting of textured and non-textured oxide layers (vol%)

Tape	Matrix powder	Al_2O_3 platelet	Dispersant*	Na alginate	Water
TA	25–30	1–6	0.15–0.2	0.5–0.6	66–72
RBAO	32–38	0	0.15–0.2	0.5–0.6	62–68
ATZ	25–30	0	0.2–0.25	0.6–0.7	70–75
RBM	28–32	0	0.2–0.25	0.5–0.6	68–72

* DISPEX A40, Allied Colloid, England

parallel-beam assembly (PW1710 based). The data were recorded for 2θ values from 40 to 154° using Cu $K\alpha_1$ radiation with a step size of 0.05° and a 3-s scan time per step. The lower limit of 40° was chosen to ensure a constant irradiated volume for all data. The integrated intensities for all reflections were calculated using PHILLIPS APD software.

The March–Dollase function [28], $P_r(\eta)$, was used to estimate the probability of observing diffraction from the hkl planes at a given angle:

$$P_r(\eta) = (r^2 \cos^2 \eta + r^{-1} \sin^2 \eta)^{-3/2} \quad (2)$$

where η is the angle between the basal plane (001) and the (hkl) planes. The parameter r is the 'compaction ratio' (final thickness/initial thickness) in the original March model. For the present purpose, r was used to indicate the degree of texture: $r = 1$ for a random sample and $r < 1$ for a textured sample. The March–Dollase function satisfies the following normalized equation [29]

$$\int_0^{2\pi} \int_0^{\pi/2} P_{hkl}(\eta, \phi) \sin \eta \mathrm{d}\eta \mathrm{d}\phi = 2\pi \quad (3)$$

where $P_{hkl}(\eta, \phi)$ is the polar axis density function, ϕ is the in-plane rotation angle, and η is the tilt angle about an axis in the plane of diffraction and perpendicular to the is ϕ axis. $P_r(\eta)$, is therefore a multiple of the random distribution (MRD) in an isotropic polycrystal. In the present case of axisymmetric texture Eq. 3 simplifies to

$$\int_0^{\pi/2} P_{hkl}(\eta) \sin \eta \mathrm{d}\eta = 1 \quad (4)$$

After normalizing the polar density function $P_{hkl}(\eta)$ and fitting the March–Dollase function, the oriented volume fraction was calculated as the volume fraction of crystallites oriented in directions for which $P > 1$ (greater than random). The oriented volume fraction was thus defined as:

$$V_{\text{oriented}} = \int_0^{\eta_1} (P(\eta) - 1) \sin \eta \mathrm{d}\eta \quad (5)$$

where η_1 is given by $P(\eta_1) = 1$.

Microtexture was also investigated using electron back-scatter diffraction (EBSD) in the LEO 982-FEG-SEM. Surface preparation for the EBSD sample is critical since the diffraction information originates in a 20 nm layer at the surface, corresponding to the penetration depth for back-scattered electrons. In our process, the sample surface was polished, etched, and ultrasonically cleaned before EBSD examination. The EBSD data were collected sequentially by positioning the focussed electron beam on each grain individually. The normal to the sample surface was tilted 70° to the incident beam and the EBSD pattern was captured at a beam voltage of 20 kV. The individual crystal orientations were analyzed using commercial software to generate discrete pole figures for each localized, microtexture data set.

Results and discussion

Texture control in *c*-axis TA interlayers

A cross-section of gel-cast green tape is shown in Fig. 1 and demonstrates alignment of the alumina seed platelets by the gel casting process. Good alignment of the seed alumina platelets is a key factor in attaining high particle packing density in the green bodies, and the aligned, high aspect ratio platelets did not prevent the achievement of high green densities in the uniaxially and cold-isostatically pressed compacts. High sintered densities were obtainable in the TA samples after sintering at 1550 °C for 2 h, despite the presence of the aligned platelets and the limitations of pressureless sintering. As expected, under the same sintering conditions lower final densities were associated with higher initial platelet contents.

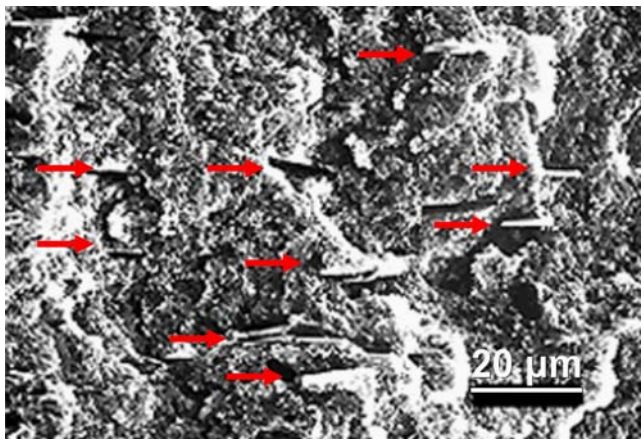

Fig. 1 SEM image of a cross-section of gel-cast textured green tape showing the distribution of seed platelets (marked by arrows) in the tape

The linear shrinkage ratios (the ratio of the sintering shrinkage of the compact perpendicular and parallel to the original seed platelets) were also measured, as shown in Fig. 2. Increasing the initial platelet content leads to increased constraint in the plane of the platelets, so that more densification occurs normal to the platelets. Thus, platelet alignment is accompanied by anisotropic densification, as has been reported for an alumina-platelet-reinforced Ce–ZrO_2/Al_2O_3 composite [30].

The volume of textured (aligned) crystals increased dramatically during sintering through growth of the aligned seed platelets at the expense of the surrounding, randomly oriented, fine Al_2O_3 particles [2]. The microstructure of a cross-section of a sintered alumina compact with 4.8 vol% initial seed platelet content is shown in Fig. 3 and the microstructural anisotropy of the monolithic TA is evident in both the optical micrograph in Fig. 3a and the SEM image in Fig. 3b. The seed platelets have acted as templates for both sintered grain morphology and crystalline texture development, so that the strong 0001 texture (*c*-axis perpendicular to the sample surface and normal to the tape-casting direction) is accompanied by morphological anisotropy (flattened grains parallel to the surface). Figure 3c shows a bright-field TEM image taken from a cross-section of TA layer, in which a grain boundary between two TA grains is accurately parallel to both basal planes (see inserted SAD pattern) with no sign of any glassy phase or second-phase precipitation.

X-ray diffraction patterns from a green body and sintered (1550 °C, 2 h) samples with different initial platelet contents are shown in Fig. 4. The 00.6 and 00.12 peaks for the sintered, platelet-containing samples are much more prominent than those from either the green body or a sintered, platelet-free sample. Similarly, the near-basal-plane peaks, such as 10.10 and

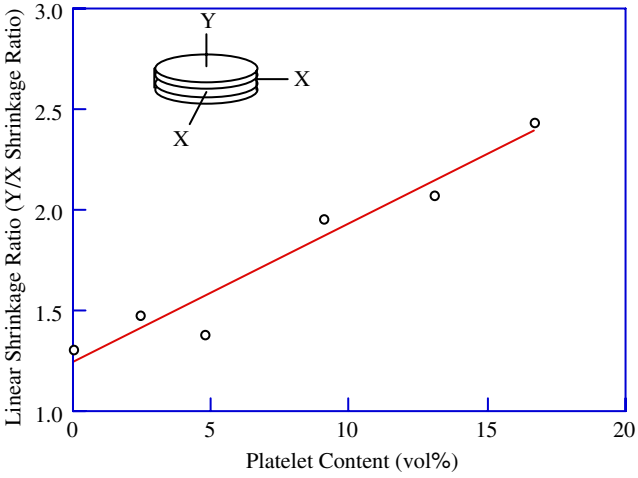

Fig. 2 Linear shrinkage ratios for the textured alumina (TA) samples with different initial seed platelet contents

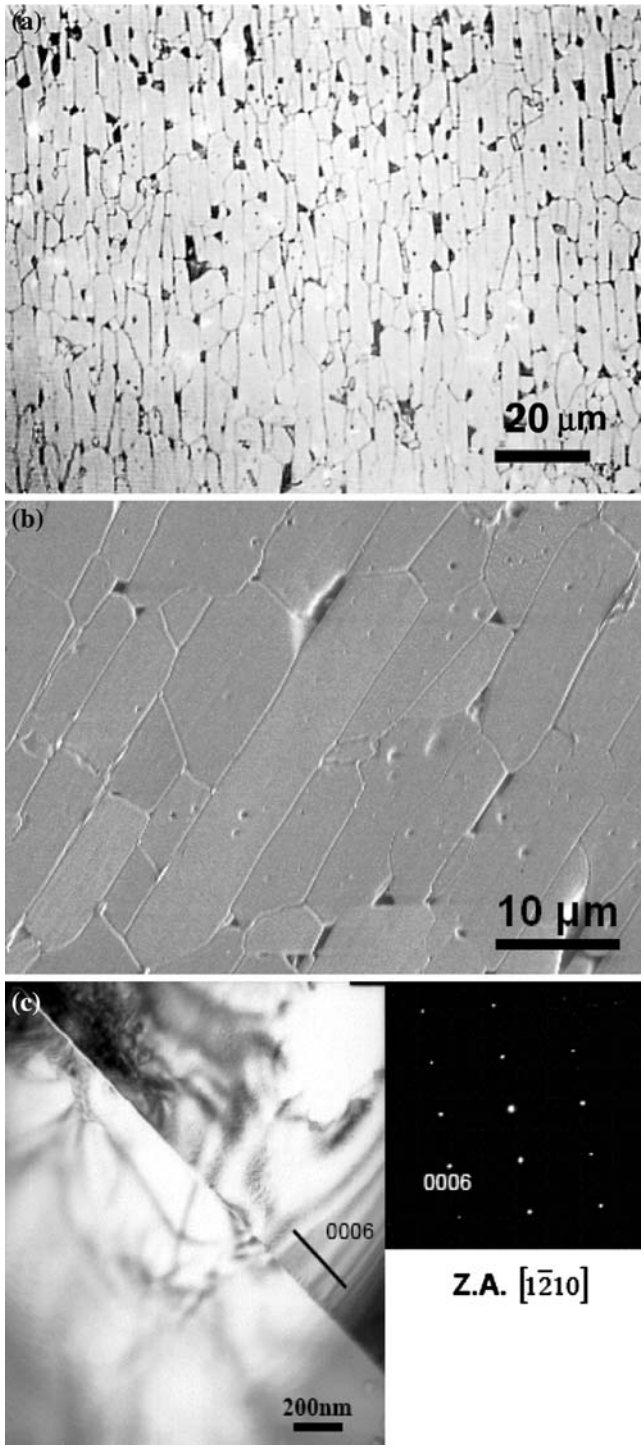

Fig. 3 (**a**) Optical micrograph of the cross-section of fully sintered textured alumina (TA) with 4.8 vol% initial platelets; (**b**) SEM micrograph of the cross-section of fully sintered TA with 4.8 vol% initial platelets; (**c**) bright-field TEM image of a basal grain boundary between two TA grains

10.14 (17.5° and 12.7° from the basal plane, respectively), also appear stronger in the platelet-containing samples than in the green body or the platelet-free sample. The results confirm that large volume fractions of strong *c*-axis textured material are formed in sintered platelet-containing samples. Diffraction data from samples with different initial platelet contents were compared with the diffraction data from a platelet-free, random sample. The MRD for each reflection was calculated and fitted to a March–Dollase model function $P_{hkl}(\eta)$, and is shown as a function of η in Fig. 5a. The parameter r in the March–Dollase function and the oriented volume fraction calculated from Eq. 5 are plotted as a function of η in Fig. 5b, from which the smallest r value and the highest oriented volume fraction are seen to correspond to an initial platelet fraction of 9.1 vol%. In effect, the degree of crystallographic alignment initially increases with increasing platelet content but eventually reaches a maximum due to increasing interference between adjacent platelets as they rotate into the plane of the tape during tape-casting. Interference between neighboring platelets is also the probable cause of the lower densification at high platelet contents.

In traditional texture determination by X-ray diffraction, large numbers of grains are sampled simultaneously and no information is available regarding the crystal location responsible for individual X-ray reflections. Local grain orientation cannot be identified by the X-ray method. Transmission electron microscopy (TEM) is capable of providing diffraction data from grains down to 10 nm diameter with an angular precision, in convergent beam diffraction, as high as 0.1°. However, TEM specimens must be electron

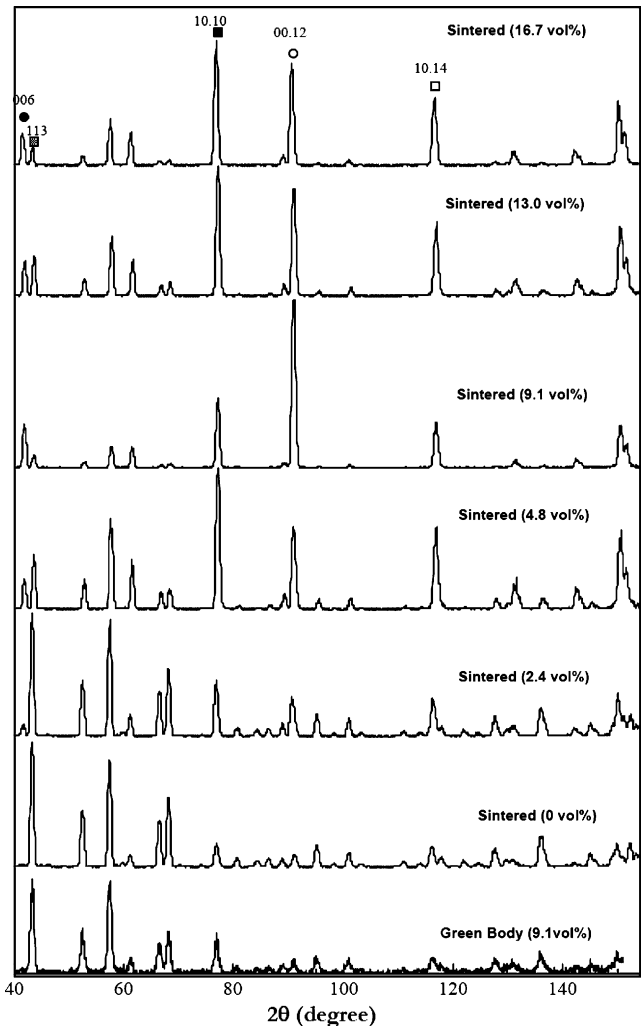

Fig. 4 XRD patterns for green and sintered alumina samples with different initial seed platelet contents

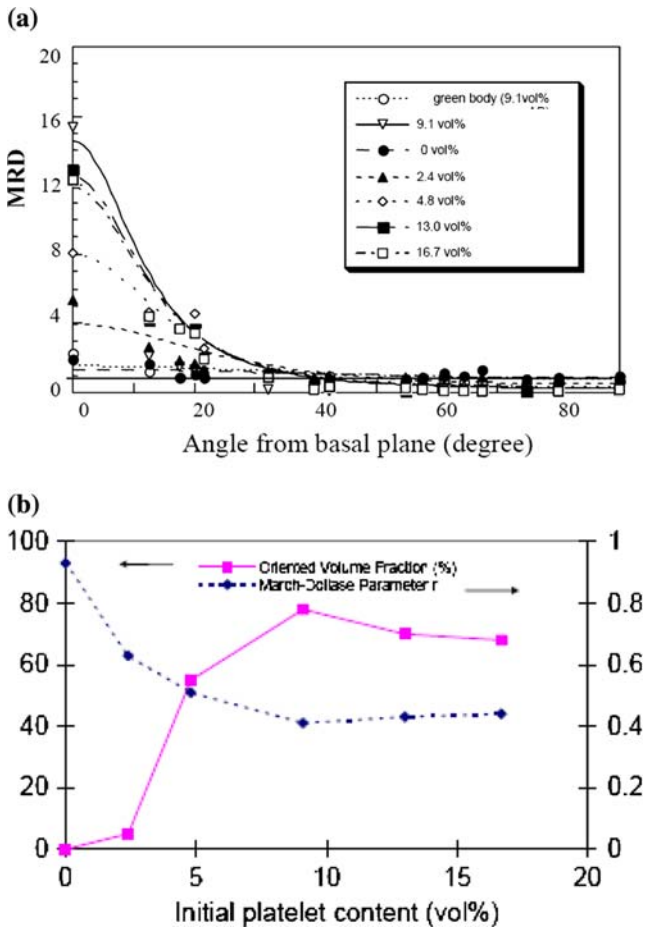

Fig. 5 (**a**) The multiple of random distribution (MRD) for observed (hkl) reflections from textured alumina (TA) samples with different initial platelet contents, together with the March–Dollase function fitting; (**b**) the March–Dollase parameter *r* and the oriented volume fractions for TA samples as a function the initial platelet content

transparent, typically less than 100 nm thick, and the area of the sample thin enough for electron transmission is only of the order of the typical grain size of TA, so that TEM unsuitable for comparing grain orientations in these materials. In the present work EBSD was used to examine the regional grain orientation relations (microtexture) in the *c*-axis textured α-alumina pellets. Figure 6a shows a forward-scatter secondary electron (FSE) image taken from an area examined in a tilted in-plane surface of the TA with 9.1% initial platelet content. A dozen alumina grains from this area (marked by letters) were examined by EBSD and a standard EBSD pattern, shown in Fig. 6b, was first taken from a polished sapphire substrate for comparison. Figure 7 shows the EBSD patterns taken from the TA grains and the EBSD results demonstrate that the local orientation of each grain relative to the surface normal deviates only slightly from the 0001 zone axis. These results were plotted in the orientation of the plane of the sample as discrete and inverse pole figures shown in Fig. 8. The above EBSD measurement results confirm the X-ray diffraction macrotexture results and show the strong out-of-plane *c*-axis texture. In addition, no preferred in-plane orientation was detected from the EBSD measurement. Similar results can also be obtained from EBSD characterization of the cross-section of the same TA sample (not shown).

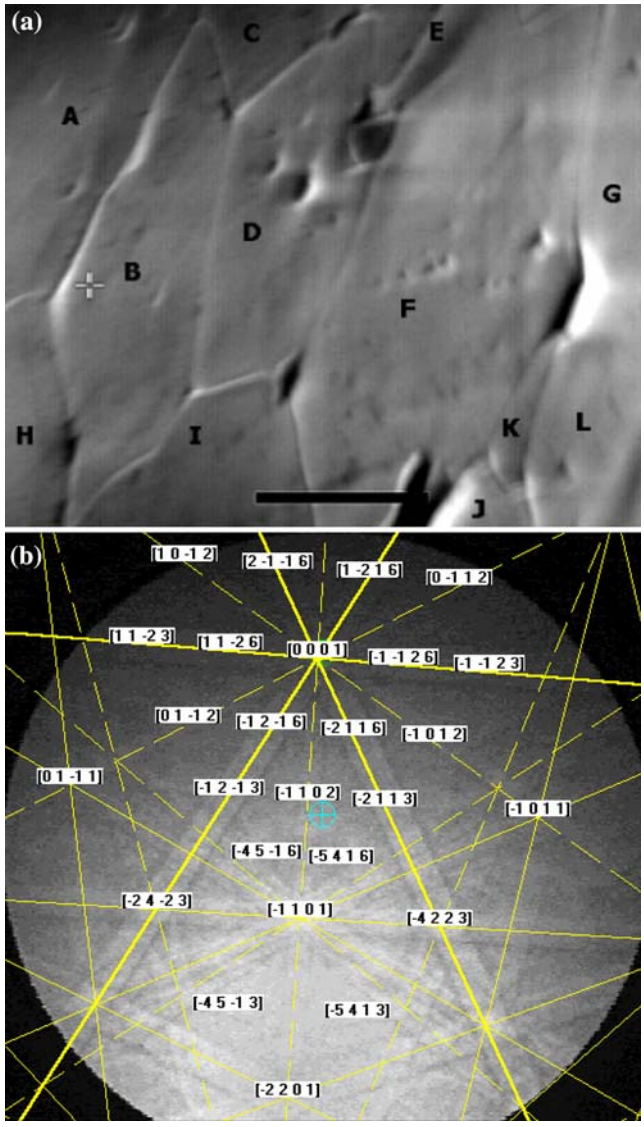

Fig. 6 (**a**) Forward-scatter secondary electron (FSE) image taken from an area examined in a tilted in-plane surface of the textured alumina (TA) with 9.1% initial platelet content; (**b**) indexed standard electron back-scatter diffraction (EBSD) pattern from polished a basal sapphire substrate

Formation of RBAO/TA, ATZ/TA, and RBM/TA laminates

Based on the above texture analysis, we decided to use 9.1 vol% alumina platelets in the TA interlayers in all three types of laminates. These TA tapes were first used, together with texture-free, fine-grain, RBAO alumina layers, to fabricate the RBAO/TA laminate, in which the two 'different' layers contain the same phase, α-alumina, but in different morphologies. The thermal mismatch between the textured and non-textured layers in this laminate is small, and is associated with the 10% difference in thermal expansion coefficient of α-alumina parallel and perpendicular to the *c* axis. The textured layers in this laminate structure are expected to reinforce the alumina by crack deflection along the grain boundaries formed with the basal planes of the textured grains, which leads to the formation of low energy basal plane free surfaces.

In order to adapt traditional RBAO processing for the texture-free layers in this texture-reinforced, single-phase alumina laminate, a fine (usually submicron) precursor powder mixture of aluminum and alumina was prepared by attrition milling. The particle size distribution after attrition milling is shown in Fig. 9a, while Fig. 9b and c compare the as-received aluminum powder (plasma-sprayed, 45–90 μm) with the submicron particle size and irregular grains in the attrition milled RBAO powder mixture. The heating cycle for RBAO samples requires a low heating rate below 1100 °C to ensure sufficient oxidation of the metal particles. Phase evolution in a series of RBAO samples was evaluated by X-ray diffraction. After heating at 1 °C/min to 1100 °C, the RBAO sample was fully oxidized to α-alumina, but a large fraction of the metal oxidized below the melting point (660 °C). Figure 10a shows the X-ray diffraction patterns from a RBAO

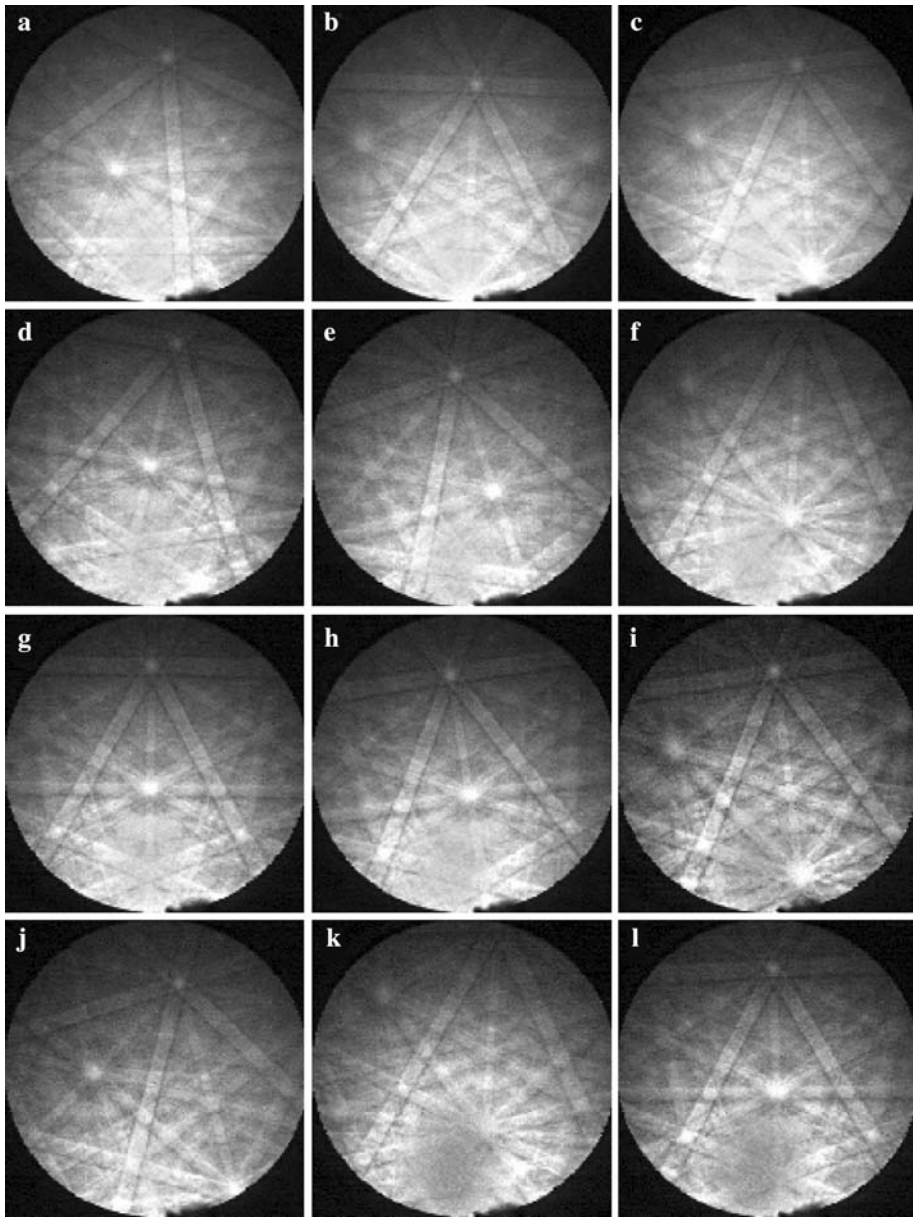

Fig. 7 Electron back-scatter diffraction (EBSD) patterns from the 12 grains (A–L) indicated in Fig. 6

sample (20 vol% Al) before and after reaction bonding, confirming complete oxidation after the RBAO process. The final density of the RBAO/TA laminates reached 97% TD. Figure 10b shows a typical optical micrograph of a sintered RBAO/TA laminate, in which the thickness ratio of RBAO and TA layer is 3:1 (alternating three stacks of gel-cast green RBAO tapes and one gel-cast green TA tape). It has been found that the resulting laminar interfaces are fairly straight in the laminate sample.

The second type of the texture-reinforced ceramic laminate was developed from a fine-grain, texture-free, ATZ matrix interleaved with highly TA interlayers. In contrast to the above RBAO/TA laminates, the ATZ layers are now in tension while the TA layers are in compression, due to thermal expansion mismatch between the adjacent layers. The residual stress distribution is therefore expected to enhance crack deflection at the interface between the zirconia and TA layers.

Figure 11a shows an optical micrograph of a sintered ATZ/TA laminate, in which the thickness ratio of ATZ and TA layer is 1:1 (alternating one gel-cast green ATZ tape and one gel-cast green TA tape). The ATZ layer thickness has been found to be slightly smaller than that of TA layer, which is due to larger

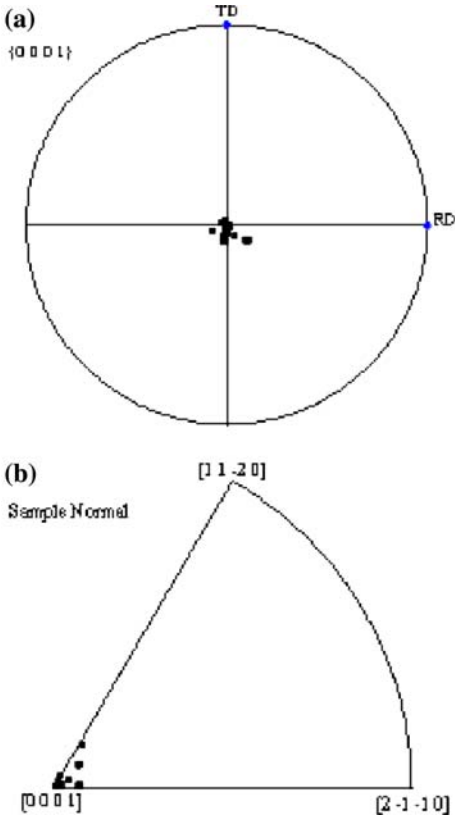

Fig. 8 Discrete 0001 pole figure (**a**) and inverse pole figure (**b**), both measured from electron back-scatter diffraction (EBSD) data

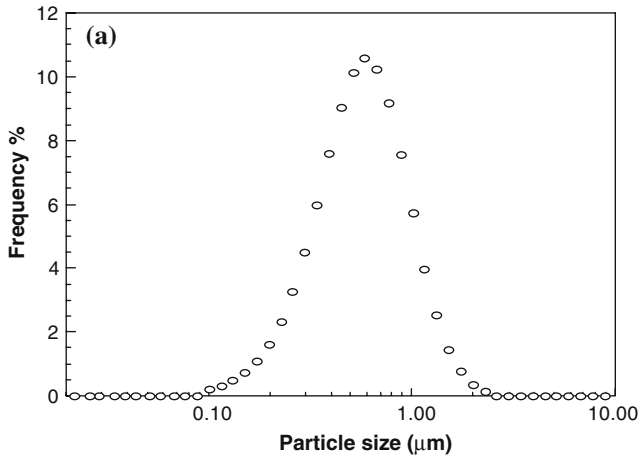

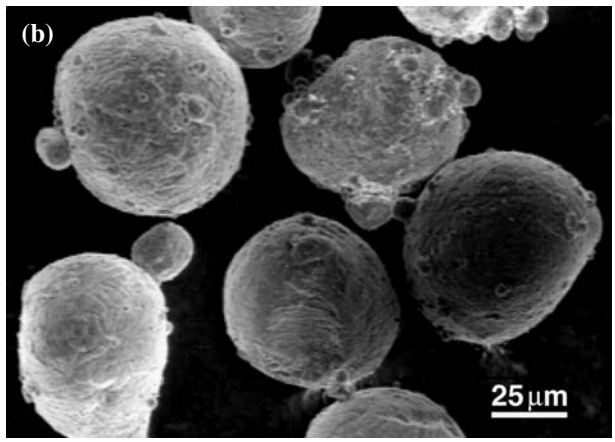

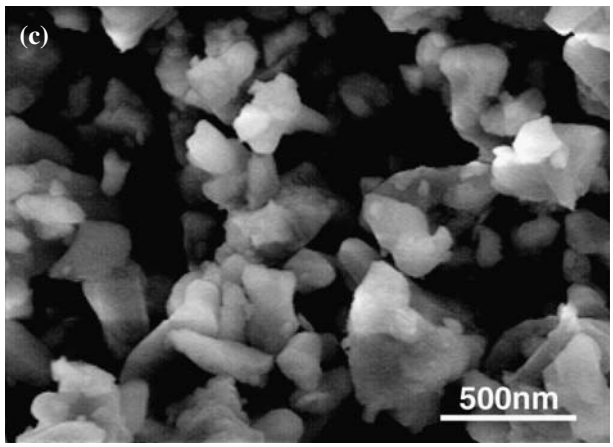

Fig. 9 (**a**) Particle size distribution for the reaction-bonded aluminum oxide (RBAO) powder mixture after attrition milling; (**b**) The as received Al metal powder; (**c**) The RBAO powder mixture after attrition milling

sintering shrinkage through original tape thickness in ATZ layer. Figure 11b–d show a SEM image and EDX composition maps taken from fine grain ATZ layer. The results indicate that the alumina grains are uniformly distributed among the zirconia matrix in the ATZ layer.

For the RBM/TA laminate, the mullite layers were produced by an in situ mullitization reaction. In contrast to the RBAO/TA and ATZ/TA laminates, the TA layers are now designed in biaxial tension due to the thermal mismatch between adjacent layers, placing the mullite in residual compression. The expectation was that the mullite layers would be reinforced by the imposed compressive stresses, while the TA microstructure would still promote crack deflection along the basal plane grain boundaries. Figure 12a shows an optical micrograph of the cross-section of a sintered RBM/TA laminate, in which the thickness ratio of RBM and TA layer is 1:1 (alternating one gel-cast green RBM tape and one gel-cast green TA tape).

As in the RBAO process, the precursor particle size is critical for the successful completion of the RBM reaction. With a coarse zircon powder, the reaction between zircon and alumina will be difficult to complete, and Fig. 12b shows a large unreacted zircon grain in the RBM layer. Phase evolution in RBM samples with different zircon precursor particle sizes was therefore studied by X-ray diffraction analysis. The phase contents of both zirconia (M_1) and mullite (M_2) were estimated using the following equations:

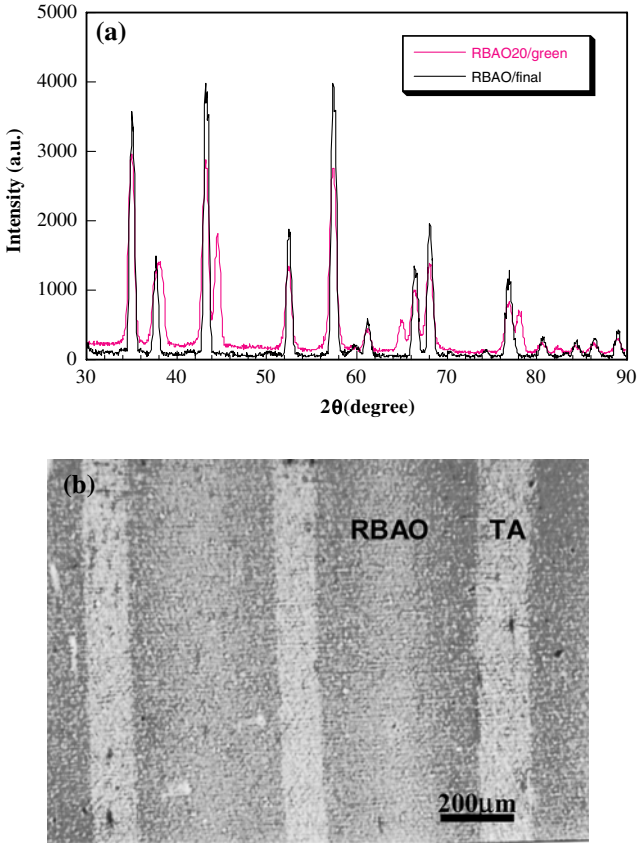

Fig. 10 (**a**) XRD powder patterns from a reaction-bonded aluminum oxide (RBAO) sample before and after reaction bonding; (**b**) optical micrograph of the cross-section of a RBAO/TA laminate

$$M_1 = \frac{I\{m\text{–}ZrO_2(111)\}+I\{t\text{–}ZrO_2(111)\}}{I\{m\text{–}ZrO_2(111)\}+I\{t\text{–}ZrO_2(111)\}+I\{ZrSiO_4(200)\}} \quad (6)$$

$$M_2 = \frac{I\{\text{Mullite}\,(210)\}}{I\{\text{Mullite}\,(210)\}+I\{ZrSiO_4(200)\}} \quad (7)$$

The results are summarized in Table 3. With a sub-micron zircon as starting powder, the reaction between zircon and alumina was much closer to completion than for the case of coarse zircon powder. As shown in Fig. 12c, the RBM layer made from finer zircon powder is composed of only mullite (matrix) and zirconia (brighter and in round shape) grains. From the XRD results, it has been found that up to 95% of the zircon was reacted to form mullite and zirconia. The final laminate density was estimated to be 93–95 TD% by comparing the results of X-ray phase analysis with the density measurements. However, it should be noted that some glassy phase may be present in the RBM layers, which would not be detected by XRD and would reduce the residual porosity.

The above results show that we have successfully fabricated three types of oxide ceramic laminates, which were designed for different stress states and are

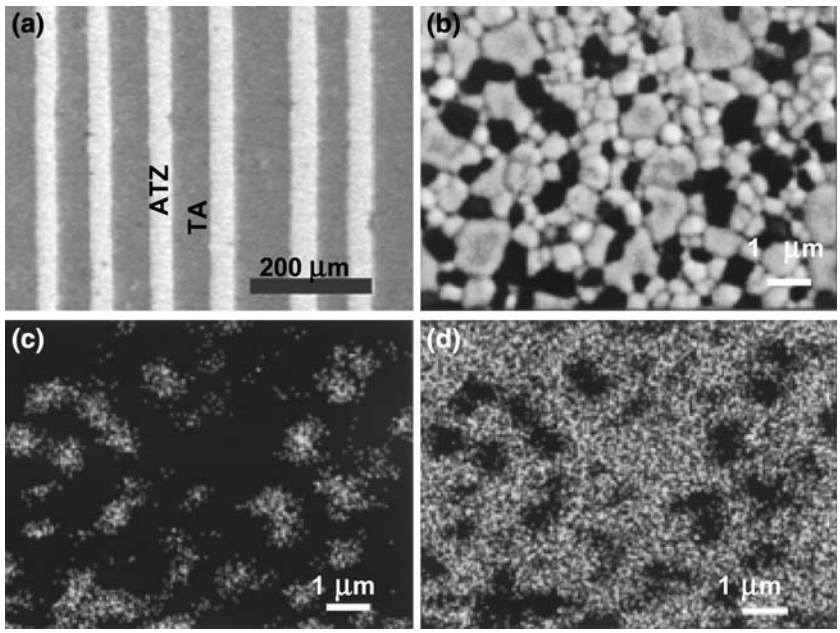

Fig. 11 (**a**) Optical micrograph of the cross-section of a sintered alumina-toughened zirconia/textured alumina (ATZ/TA) laminate; (**b**) back scattering electron image of the ATZ layer; (**c**) Al energy dispersive X-ray spectroscopy (EDS) map of the ATZ layer; (**d**) Zr EDS map of the ATZ layer

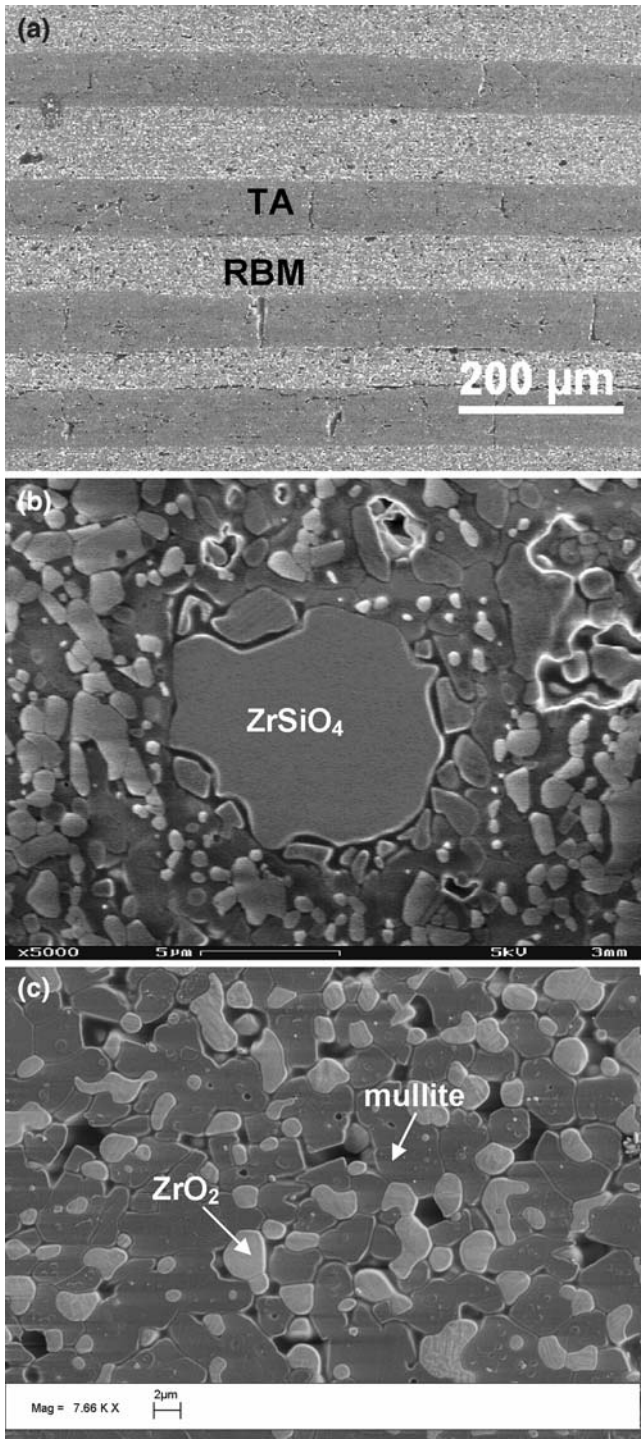

Fig. 12 (**a**) Optical micrograph of the cross-section of a sintered reaction-bonded mullite/textured alumina (RBM/TA) laminate; (**b**) SEM image of a large unreacted zircon grain in an RBM layer, in which larger initial zircon powder was used; (**c**) SEM image of the RBM layer made from finer initial zircon powder

all based on TA interlayers. The detailed microstructural characterisation and mechanical behaviour will be discussed in the next paper.

Table 3 Phase evolution in RBM layers

Reaction temp (°C)	M_1 ratio		M_2 ratio	
	Fine zircon (<1 μm)	Coarse zircon (~5 μm)	Fine zircon (<1 μm)	Coarse zircon (~5 μm)
0	0	0	0	0
1300	0	0	0	0
1400	0	0	0	0
1450	0.15	0.10	0.12	0.10
1500	0.52	0.21	0.35	0.20
1550	0.70	0.29	0.67	0.27
1600	0.97	0.42	0.93	0.29

Conclusions

Three classes of texture-reinforced ceramic laminates with strongly bonded interfaces have been successfully fabricated: a reaction-bonded, single-phase alumina/textured alumina laminate (RBAO/TA), a ATZ/TA laminate, and a RBM/TA laminate. Gel casting was successfully used to produce preform tapes for both the highly TA interlayers and for the texture-free matrix layers in all three laminate systems. These three laminate systems are all based on highly TA interlayers, but with significantly different thermal expansionl mismatch between the laminate matrix composition and the TA interlayers. The textured layers have *c*-axis symmetry, with the strongest texture, calculated to be 60–80% from the March–Dollase model, obtained from initial 9.1 vol% platelet content. Fewer platelets were insufficient to ensure oriented grain growth throughout the textured layer, while more platelets inhibited platelet alignment.

Acknowledgements This work was supported by AFIRST (French-Israel Association for Scientific and Technological Research) under contract #6052194. The authors would like to acknowledge the previous work of Thierry Carisey who pioneered the concept of texture control in tape-cast alumina while supported by the Government of France as a CSN at Technion. The authors would also like to thank Dr. Suxing Wu for his unstinting help in developing RBAO and RBM processing for laminated systems.

References

1. Paulik SW, Faber KT, Fuller ER (1994) J Am Ceram Soc 77:454
2. Carisey T, Laugier-Werth A, Brandon DG (1995) J Euro Ceram Soc 15:1
3. Vedula VR, Glass SJ, Saylor DM, Rohrer GS, Carter WC, Langer SA, Fuller ER (2001) J Am Ceram Soc 84:2947
4. Ma Y, Kruger KL, Bowman KJ (1991) J Am Ceram Soc 74:2941
5. Lee F, Sandlin MS, Bowman KJ (1993) J Am Ceram Soc 76:1793

6. Pentecost JL, Wright CH (1963) Adv X-Ray Anal 7:174
7. Zimmerman MH, Faber KT, Fuller ER (1997) J Am Ceram Soc 80:2725
8. Baskin DM, Zimmerman MH, Faber KT, Fuller ER (1997) J Am Ceram Soc 80:2929
9. Hirao K, Nakaoka T, Brito ME, Kanzaki S (1994) J Am Ceram Soc 77:1857
10. Hong SH, Cermignani W, Messing GL (1996) J Euro Ceram Soc 16:133
11. Sacks MJ, Scheiffele GW, Staab GA (1996) J Am Ceram Soc 79:1611
12. Seabaugh MM, Kerscht IH, Messing GL (1997) J Am Ceram Soc 80:1181
13. Suvaci E, OH KS, Messing GL (2001) Acta Mater 49:2075
14. Clegg WJ, Kendall K, Alford NM, Button TW, Birchall JD (1990) Nature 347:455
15. Davis JB, Kristoffersson A, Carlström E, Clegg WJ (2000) J Am Ceram Soc 83:2369
16. Gee IA, Dobedoe RS, Vann R, Lewis MH, Blugan G, Kuebler J (2005) Adv Appl Ceramics 104(3):103
17. Cai PZ, Green DJ, Messing GL (1998) J Eur Ceram Soc 5:2025
18. Rao MP, Sánchez-Herencia AJ, Beltz GE, McMeeking RM, Lange FF (1999) Science 286:102
19. Hatton B, Nicholson PS (2001) J Am Ceram Soc 84:571
20. Claussen N, Le T, Wu S (1989) J Euro Ceram Soc 5:29
21. Claussen N, Travitzky NA, Wu S (1990) Ceram Eng Sci Proc 11:806
22. Wu S, Holz D, Claussen N (1993) J Am Ceram Soc 76:970
23. Claussen N, Wu S, Holz D (1994) J Euro Ceram Soc 14:97
24. Boch P, Giry JP (1985) Mater Sci Eng 71:39
25. Harris GB (1952) Philos Mag 43:113
26. Barrett CS, Massalski TB (1978) Structure of metals, crystallographic methods, principles and data, 3rd ed. Permagon Press, New York
27. Valvoda V, Järvinen M (1990) Powder Diffraction 5:200
28. Dollase WA (1986) J Appl Cryst 19:267
29. Cline JP, Vaudin MD, Blendell JE, Handwerker CA, Jiggetts R, Bowman KJ, Medendorp N (1994) Adv X-Ray Anal 37:473
30. Roeder RK, Trumble KP, Bowman KJ (1997) J Am Ceram Soc 80:27